Vortex Harmonic Generation by Circularly Polarized Gaussian Beam Interacting with Tilted Target

Lingang Zhang,[1] Baifei Shen,[1,2,*] Zhigang Bu,[1] Xiaomei Zhang,[2] Liangliang Ji,[1] Shan Huang,[1,3] M. Xiriai,[2] Zhangli Xu,[1,3] Chen Liu,[4] and Zhizhan Xu[1]

[1] *State Key Laboratory of High Field Laser Physics and CAS Center for Excellence in Ultra-intense Laser Science, Shanghai Institute of Optics and Fine Mechanics (SIOM), Chinese Academy of Sciences (CAS), Shanghai 201800, China*

[2] *Department of Physics, Shanghai Normal University, Shanghai 200234, China*

[3] *Center of Materials Science and Optoelectronics Engineering, University of Chinese Academy of Sciences, Beijing 100049, China*

[4] *Department of Computer Information and Cyber Security, Jiangsu Police Institute, Nanjing, Jiangsu 210031, China*

(Received 20 January 2021; revised 6 June 2021; accepted 7 July 2021; published 28 July 2021)

When a circularly polarized (CP) Gaussian beam normally irradiates a solid plasma target, the spin angular momentum of the CP beam transforms into the orbital angular momentum (OAM) of the high-order harmonics through the spin-orbital interaction; this provides a promising way to obtain intense attosecond pulses carrying OAM. However, normal irradiation faces realistic challenges in experiments, as one cannot extract the harmonic without interfering with the driving laser. Here, we propose a feasible scheme to generate vortex high-order harmonics by using a CP Gaussian beam obliquely incident to the target. Theoretical analyses and simulation results show that the nth-order harmonic is composed of vortex modes with topological charges from $l = 0$ to $|l| = n - 1$. The composition ratio depends on the laser focal size and the incident angle. The obtained number of vortex photons is comparable to the normal incidence case at up to an incident angle of 10°, which greatly facilitates the experimental arrangement.

DOI: 10.1103/PhysRevApplied.16.014065

I. INTRODUCTION

Studying the transition states of chemical reactions by using femtosecond spectroscopy [1] has led to the era of ultrafast dynamics, which forms the cornerstone of modern science. High-order harmonic generation (HHG) is a typical method to obtain such ultrafast probing pulses. The laser either interacts with noble gases to generate harmonics at moderate laser intensity ($\sim 10^{14-16}$ W cm^{-2}) [2–6] or with an overdense plasma target to get much stronger pulses in the relativistic regime (10^{18} W cm^{-2} and above) [7–13]. By frequency selecting, attosecond pulses are obtained and find applications in various scenarios, including ultrafast atomic and molecular dynamics [14,15], characterizing plasmas by x-ray spectroscopy [16], and extreme ultraviolet (XUV) or x-ray pump-probe techniques [17–19].

Angular momentum (AM) was recognized as an important characteristics of light after work by Poynting [20], who considered the spin AM (SAM, $\pm\hbar$ per photon, where $\hbar$ is the reduced Plank constant) produced by the circularly polarized (CP) beam. This was demonstrated in experiments by Beth [21]. Then the seminal paper by Allen *et al.* [22] started research into orbital AM (OAM), carried by vortex beams with a helical wavefront $\exp(-il\varphi)$, where l is the topological charge and φ is the azimuthal angle. Vortex beams can be produced by introducing a vortex phase into a Gaussian pulse through a q plate [23] or other optical elements [22,24]. In the relativistic regime, this can be accomplished by using plasma-based methods [25–28]. The amplification of seed vortex beams to high energy [29,30] is also in progress. Since a vortex beam carries OAM of $l\hbar$ per photon, which can be much larger than the SAM, it has been exploited in various applications, ranging from optical manipulation [31,32], imaging [33], and quantum optics [34] to optical communication [35].

Governed by the conservation laws of AM, energy, and momentum, it is theoretically indicated and experimentally verified that the HHG driven by a linearly polarized (LP) vortex beam produces an nth-order harmonic with $nl\hbar$ OAM per photon [36–39]. For the CP beam, according to the relativistic oscillating mirror (ROM) model [8–10], it was initially believed difficult to drive solid HHG in normal incidence because the ponderomotive force of a plane wave does not contain the oscillating term. The HHG is

*bfshen@mail.shcnc.ac.cn

shown to be possible for a few-cycle relativistic CP laser interacting with near-critical-density plasmas [40]. At solid densities, the HHG process is suppressed at normal incidence. However, it was reported recently [41] that, by irradiating a solid target with a tightly focused intense CP Gaussian laser, the SAM of the driver can be converted into the OAM of the harmonics. The driving source is the vortex longitudinal component of the tightly focused CP Gaussian beam [42,43] induced by the spin-orbital interaction [44], which was also found in other phenomena, such as spin-Hall effects [45], spin-dependent effects in nonparaxial fields [46], and evanescent waves [47]. Other studies utilizing a predenting target [48], waveguide [49], and aperture target [50] to facilitate spin-orbital interactions have also been explored.

Using the CP laser pulse instead of the vortex laser provides a practical method to obtain vortex harmonics. However, the normal-incidence configuration faces realistic limitations in experiments. It is quite challenging to extract the vortex harmonic without interfering with the incident laser beam. The intense beam backtrack from the target may also harm the laser system.

Here, we study vortex harmonic generation using a CP Gaussian laser obliquely incident onto a plasma surface and illustrate vortex CP harmonics generation. With theoretical analyses and full three-dimensional (3D) simulations, we demonstrate that the vortex harmonics and regular Gaussian harmonics coexist in the same harmonic order. The nth-order harmonic is composed of vortex modes with topological charge from $l = 0$ (Gaussian) to $|l| = n - 1$. By using the azimuthal Fourier (inverse) transform, the mode constitution is obtained and the pure vortex mode can be well extracted. Compared with the normal incidence [41,48], we find quite different phenomena in the oblique configuration in our work, which greatly facilitates the experimental arrangement, and therefore, provides a more feasible way to obtain an intense attosecond OAM XUV source.

II. THEORETICAL ANALYSES

We start by considering a CP laser propagating obliquely with incident angle θ with respect to the $+x$ axis, the electric field of which can be expressed as follows:

$$\mathbf{E}_i = ik_0^{-1}\partial_r u(r)E_0 \exp[i(k_x x + k_y y - \omega_0 t - \sigma\varphi)]\mathbf{e}_\parallel + E_0 u(r)\exp[i(k_x x + k_y y - \omega_0 t)](\mathbf{e}_p - i\sigma\mathbf{e}_s), \quad (1)$$

where $k_x = k_0\cos\theta$; $k_y = k_0\sin\theta$; $k_0 = \omega_0/c$, where ω_0 is the angular frequency and c is the speed of light in vacuum; $u(r) = \exp(-r^2/w_0^2)$ is the spatial envelope; and w_0 is the beam waist. $\mathbf{e}_s = \mathbf{e}_z$ and $\mathbf{e}_p = -\mathbf{e}_x\sin\theta + \mathbf{e}_y\cos\theta$ are unit vectors representing the two orthogonal transversal components, and $\mathbf{e}_\parallel = \mathbf{e}_x\cos\theta + \mathbf{e}_y\sin\theta$ denotes the longitudinal vortex component induced due to the finite transverse size and profile of the CP beam [41]. $\sigma = \pm 1$ represent the right- and left-handed circularly polarization (defined from the point of view of the receiver), respectively; φ is the azimuthal angle for the vortex component.

This CP laser beam impinges on the plasma surface located at $x = 0$; the latter is driven by the incident and reflected beam, i.e., $\mathbf{E}_d = \mathbf{E}_i + \mathbf{E}_r$. According to the ROM model [8–10], the harmonics are emitted from the oscillating transverse current from the plasma surface generated via the collective transverse quiver of electrons driven by the transverse laser field, $\mathbf{J}_\perp \sim \mathbf{E}_{d\perp}$. The longitudinal component of the laser field drives the current to oscillate longitudinally, and then, the harmonics are emitted. Therefore, we separate $\mathbf{E}_d$ into transversal and longitudinal components as follows:

$$\begin{aligned} E_x &= -2E_0u(r)\sin\theta\cos(k_x x)\cos(k_y y - \omega_0 t) - 2k_0^{-1}\partial_r u(r)E_0\cos\theta\cos(k_x x)\sin(k_y y - \omega_0 t - \sigma\varphi),\\ E_y &= -2E_0u(r)\cos\theta\sin(k_x x)\sin(k_y y - \omega_0 t) - 2k_0^{-1}\partial_r u(r)E_0\sin\theta\sin(k_x x)\cos(k_y y - \omega_0 t - \sigma\varphi),\\ E_z &= 2\sigma E_0 u(r)\sin(k_x x)\cos(k_y y - \omega_0 t). \end{aligned} \quad (2)$$

The fact that E_x contains both vortex and nonvortex terms suggests that the plasma target will oscillate in mixed mode and emit mixed-mode harmonics. Additionally, through the deficiency of the oscillating term, the slow-varying ponderomotive force (light pressure) of the CP beam dents the plasma to give a curved surface. In such a case, the transversal components, $E_{y,z}$, will also exert a vortex driving force on the local deformed target [48], which serves as another vortex driving source for harmonic generation.

The reflected laser field observed at $t, x < 0$ is emitted at a retarded time $t_{\rm ret} = t - [X(t_{\rm ret}) - x]/c$ from the oscillating source, where $X(t_{\rm ret})$ is the position of the source at time $t_{\rm ret}$. We approximate the surface motion as a superposition of harmonic oscillation driven by the E_x field in Eq. (2):

$$X(t_{\rm ret}) = -X_1\sin(\omega_0 t_{\rm ret} + \sigma\varphi) - X_2\cos(\omega_0 t_{\rm ret}). \quad (3)$$

X_1 and X_2 are oscillating amplitudes related to the strength of the vortex and nonvortex term in the E_x field, respectively. This oscillating surface modifies the phase of the reflected beam due to the relativistic Doppler effect; thus, the electric field, $E_z(t)$, can be written as [9]:

$$E_z(t) \sim \sigma \cos[\omega_0 t - k_0 X(t_{\mathrm{ret}})]. \tag{4}$$

For relativistic intensities of $a_0 > 1$, the amplitude of the plasma-surface motion is very small compared with the wavelength of the laser, $X_{1,2} < \lambda_0/(4\pi)$, so we have $k_0 X_{1,2} \ll 1$. Equation (4) can be approximately derived as

$$\begin{aligned} E_z(t) &\sim \sigma \cos[\omega_0 t + \epsilon_1 \sin(\omega_0 t + \sigma\varphi) + \epsilon_2 \cos(\omega_0 t)] \\ &= \frac{\sigma}{2}\left[e^{i\omega_0 t} e^{i\epsilon_1 \sin(\omega_0 t + \sigma\varphi)} e^{i\epsilon_2 \cos(\omega_0 t)} + \text{c.c.}\right], \end{aligned} \tag{5}$$

where $\epsilon_{1,2} = k_0 X_{1,2}$ and c.c. is the complex conjugate. Employing the Jacobi-Anger identity [51], we can get the Fourier expansion of the first term in Eq. (5):

$$\begin{aligned} \sigma e^{i\omega_0 t} e^{i\epsilon_1 \sin(\omega_0 t + \sigma\varphi)} e^{i\epsilon_2 \cos(\omega_0 t)} &= \sigma e^{i\omega_0 t} \\ \times \sum_{p=-\infty}^{\infty} J_p(\epsilon_1) e^{ip(\omega_0 t + \sigma\varphi)} &\times \sum_{q=-\infty}^{\infty} i^q J_q(\epsilon_2) e^{iq\omega_0 t}, \end{aligned} \tag{6}$$

where $J_\nu(s)$ denotes the Bessel function of the first kind. To get the nth-order harmonic, p and q should meet the condition $p + q = n - 1$ and $p, q \geq 0$, then, the spectrum of the nth-order harmonic can be derived as

$$f(\omega) = \sum_{m=0}^{n-1} i^{n-1-m} J_m(\epsilon_1) J_{n-1-m}(\epsilon_2) \sigma e^{i(n\omega_0 t + \sigma m\varphi)}. \tag{7}$$

From Eq. (7), we can see that the nth-order harmonic obtained by the CP beam obliquely impinges on the plasma target carrying vortex modes from $m = 0$ (Gaussian mode) to $m = n - 1$. The upper threshold results from the conservation of energy and angular momentum law, in such a way that n CP photons deliver a maximum of $(n-1)\hbar$ of their SAM to the OAM of the harmonic. The complex-conjugate term in Eq. (5) gives the nth harmonic with a field strength (expansion coefficients) much lower than that in Eq. (7) and can be neglected [41]. At close-to-normal incidence, the vortex term of E_y in Eq. (2) is small compared with the nonvortex term; therefore, one expects that the reflected $E_y(t)$ will have the same mode composition as that of $E_z(t)$ and there is little difference in their amplitudes. In this case, the reflected beam is generally elliptically polarized, as discussed in Ref. [52].

III. SIMULATION RESULTS

We confirm our proposed scheme by 3D particle-in-cell simulations using the EPOCH code [53]. The vortex harmonics can be generated in various laser-plasma parameters at different incident angles. We take the case of 5° as an example. As shown in Fig. 1(a), a relativistic right-handed ($\sigma = 1$) CP Gaussian laser pulse with a peak intensity of 8.6×10^{18} W cm^{-2} is obliquely incident (incident angle $\theta = 5^\circ$) on the front surface of the solid target. This corresponds to a normalized amplitude of $a_0 = eE_0/m_e c\omega_0 = 2$, where E_0 and ω_0 are the electric field amplitude and angular frequency of the laser, respectively; e, m_e, and c are the electron charge, mass, and the speed of light in vacuum, respectively. The laser beam has a temporal Gaussian profile with a full width at half maximum duration of $\tau_0 = 8.3$ fs and a focal spot of $w_0 = 2.5$ μm; $\lambda_0 = 0.8$ μm is the laser wavelength. The solid target is a preionized flat plasma foil, with an initial cold electron density of $n_0 = 5n_c$ ($n_c = 1.74 \times 10^{21}$ cm^{-3} is the critical density for laser wavelength λ_0). Its thickness is 1 μm. The incident angle of the CP laser into the simulation box is 10° with respect to the $+x$ direction, while the plasma target is placed at an incline of 5° around the z axis. In this configuration, the specular reflected beam propagates along the $-x$ direction, which facilitates AM characterization. The dimensions of the simulation box is $x \times y \times z = 14.81 \times 16.94 \times 14.77$ μm^3 and sampled by $926 \times 1059 \times 924$ cells. Each cell is cubic with a side length of $\lambda_0/50$, containing one macroparticle for both electrons and protons.

The front edge of the incident CP laser reaches the plasma target at $t \sim 43$ fs and starts being reflected. The target surface driven by the incident and reflected waves oscillates rapidly and triggers the frequency upshifting of the field until the beam is completely reflected at $t \sim 70$ fs. After that, the beam, including harmonics, propagates in free space along the $-x$ direction and its properties are well preserved (see Appendix A for the E_z component of the incident or reflected beam and the energy centroid, momentum, and AM of the electromagnetic field during the interaction process). We choose and analyze the results at a later time, $t \sim 80$ fs, when the beam propagates further to avoid interference from the electrostatic field in the plasma target.

Figure 2(a) shows the Fourier spectra of the reflected field components E_y and E_z. We see that both odd and even harmonics exist in the spectra because of the oblique incidence [52]. Harmonics up to 10th order are clearly seen. In the following, we mainly discuss the second-order harmonic by selecting the spectrum between $1.5k_0$ and $2.5k_0$, where $k_0 = 2\pi/\lambda_0$ is the laser wave number. We plot the isosurface electric field of the harmonic in Fig. 1(a), together with the integrated intensity along the $-x$ direction. We see there is a saddle point in the intensity at $y = -0.40$ μm, $z = 0.55$ μm. Furthermore, the peak intensity does not appear on the propagating axis. These characteristics indicate that the second-order harmonic is neither in pure vortex mode nor in pure Gaussian mode, but in mixed states [54].

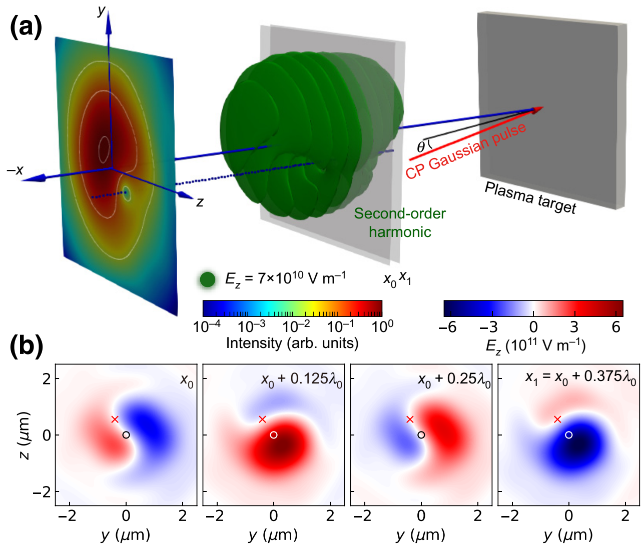

FIG. 1. (a) Schematics of proposed setup. Right, left-handed CP Gaussian laser pulse is focused onto the front surface of the plane target with incident angle $\theta = 5^\circ$, which drives the target to emit high-order harmonics. Middle, green isosurface shows electric field structure of the filtered second-order harmonic by frequency selection. Left, rainbow colors display the intensity of the second-order harmonic integrated along the propagating $(-x)$ direction. Off-axis intensity saddle point and the electric field structure indicate the mixture of Gaussian and vortex mode in the harmonic. (b) Transverse slices of the second-order harmonic electric field, E_z, during one period (0.4 μm) x_0 to x_1 as denoted in (a); crosses correspond to the off-axis intensity saddle point and circles to the x axis.

Figure 1(b) presents the E_z harmonic electric field at four cross sections between x_0 and x_1, as denoted in Fig. 1(a). The slicing points x_0 and $x_0 + 0.25\lambda_0$ are selected at the node of the wave, while the other two are at the peak and valley, respectively. At the nodes, the harmonic fields exhibit a typical vortex feature, showing two symmetric but opposite-direction lobe distributions. At the peak (valley), the fields become asymmetric. This suggests that the second-order harmonic field is composed of both Gaussian and vortex modes. At the nodes where the amplitude of the Gaussian mode is nearly zero, the vortex mode appears. However, in the peak (valley) where the Gaussian and the vortex modes both exist, their superposition results in the asymmetric field distribution.

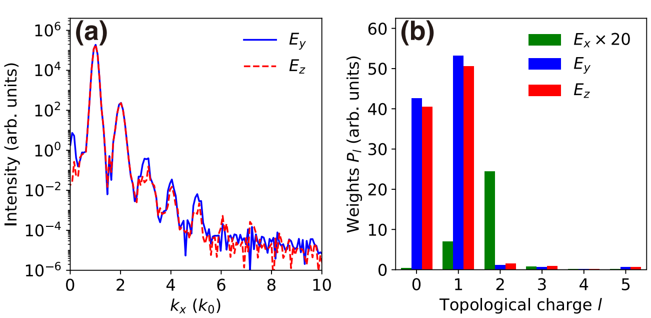

FIG. 2. (a) Spectrum of reflected electric field E_y and E_z at $y = 0$, $z = 0$. Spatial frequency is normalized by laser wave number $k_0 = 7.85 \times 10^6$ m^{-1}. (b) OAM spectrum (integrated along $-x$ direction) of the second-order harmonic obtained by azimuthal Fourier transform. Weights are all normalized to the weight of E_y to make data comparable.

To find out the mode contribution in the second-order harmonic, we transform the field $E(x,y,z)$ to cylindrical coordinates $E(x,r,\varphi)$ and then perform the azimuthal Fourier transform along the azimuthal coordinate φ, as in Ref. [55]:

$$c_l(x,r) = \frac{1}{2\pi}\int_0^{2\pi} E(x,r,\varphi)e^{il\varphi}d\varphi; \tag{8}$$

the normalized weight of each azimuthal mode l is given by the radial integration:

$$P_l(x) = \frac{\int_0^\infty |c_l|^2 r dr}{\sum_l \int_0^\infty |c_l|^2 r dr}. \tag{9}$$

Figure 2(b) represents the x-integrated OAM spectrum of the harmonic field, which is normalized by E_y. We see that, for E_y and E_z, there are two main contributions of $l = 0$ (Gaussian mode) and $l = 1$ (vortex mode), which agree well with our theoretical analyses. Additionally, the weight of the vortex mode is slightly higher than that of the Gaussian mode ($P_1/P_0 = 1.249$ for E_y and 1.247 for E_z). Meanwhile, the relative intensity of E_z is lower than that of E_y. This is because the s-component reflection is less efficient than that of p, and the reflected beam is generally elliptically polarized [52]. Due to the finite spot size and profile, the topological charge of the E_x component is $l + \sigma$ [41]. Therefore, the main contribution to E_x is the vortex mode with topological charges of $l = 1$ and $l = 2$. It is seen that OAM components up to $l = 2$ for $E_{y,z}$ and $l = 3$ for E_x are involved in building up the third-order harmonics, as shown in Appendix B. The many OAM modes of the same harmonic order indicates that they can be synthesized as structured attosecond helical beams [56], which can be applied in fields such as extreme-ultraviolet lithography [57,58], particle trapping [59], and superresolution imaging [60].

To characterize each OAM mode in the second-order harmonic, we extract the pure vortex component of the second-order harmonic (VSH) by selecting the OAM spectrum of $l \in [0.5, 1.5]$ for $E_{y,z}$ and $l \in [1.5, 2.5]$ for E_x, followed by the inverse azimuthal Fourier transform:

$$E(x,r,\varphi) = \frac{1}{2\pi}\int_0^{2\pi} c_l(x,r)e^{-il\varphi}dl. \tag{10}$$

The pure magnetic field **B** can be obtained in a similar way, and then the phases are retrieved from the electromagnetic

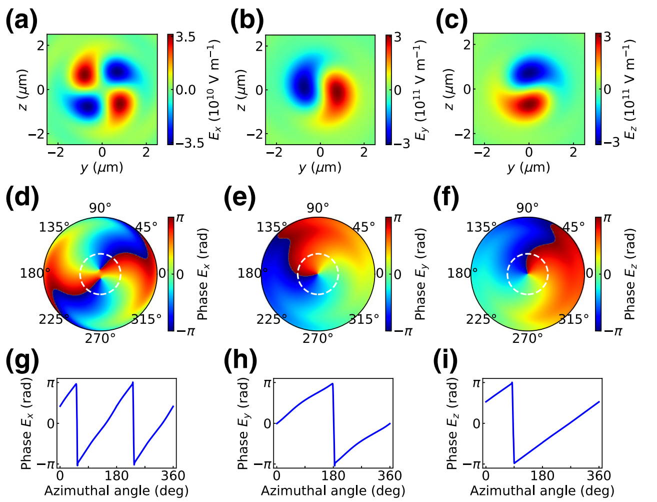

FIG. 3. Cross-section snapshot sliced at $x = -6.72$ μm for (a) E_x, (b) E_y, and (c) E_z components of the vortex $l = 1$ mode extracted from the second-order harmonic by inverse azimuthal Fourier transform, (d)–(f) demonstrate their phases, and (g)–(i) are the phase lines out at the radius of maximum intensity ($r = 0.89$ μm, white dashed circles).

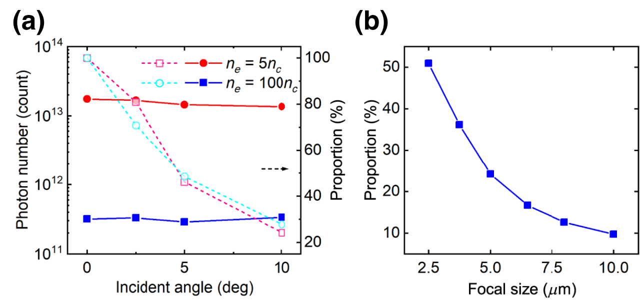

FIG. 4. (a) Photon number (solid lines) and proportion (dashed lines) of the pure vortex mode in the second-order harmonic under different incident angles and plasma densities, (b) proportion under various laser focal sizes.

field [61], as shown in Fig. 3. In experiments, extraction of the pure OAM component from the mixed mode can be achieved by sending the latter to a Mach-Zehnder interferometer with a Dove prism placed in each arm, as illustrated in [62].

The second and third columns in Fig. 3 demonstrate the field and phase distributions for the transverse components of the VSH. We see that they are consistent with the characteristics of the CP vortex mode of $l = 1$, with two-lobed field distributions. The E_y and E_z phases vary linearly from $-\pi$ to π within one cycle along the azimuthal direction, with $\pi/2$ phase difference between them [Figs. 3(h) and 3(i)]. The phase of E_x undergoes two cycles, as shown in Figs. 3(d) and 3(g), originating from circular polarization of the VSH [41,42].

Calculated by dividing the total energy, $U = \int_D \frac{1}{2}[\epsilon_0 \mathbf{E}^2 + (\mathbf{B}^2/\mu_0)]dv$, by the single photon energy, $n\hbar\omega_0$ ($n = 2$ for the VSH; the integrating space D is the whole simulation box), we get the photon numbers of the VSH and Gaussian composition of the second-order harmonic (GSH, see Appendix C), which are about $N_{\mathrm{VSH}} = 1.66 \times 10^{13}$ and $N_{\mathrm{GSH}} = 1.45 \times 10^{13}$, respectively. The total photon number for the second-order harmonic is about 3.15×10^{13}. We see that $N_{\mathrm{VSH}}/N_{\mathrm{GSH}} = 1.14$ and accounts for 98.7% of the total photons. The total angular momentum per photon of the CP VSH and GSH are $1.97\hbar$ and $0.99\hbar$, respectively. These features are in accordance with those of the OAM spectrum in Fig. 2(b).

The results presented above can be understood from the two types of electrons that exist in the oblique incident case, similar to the short and long trajectories in the HHG process in a gas target [63]. The first one has been discussed in the normal incidence case [41,48], where two ω_0 photons are absorbed and converted into one harmonic photon, delivering the SAM to the latter and forming the CP vortex beam with $l = 1$. However, one difference is that, in oblique incidence, the plasma obtains AM parallel to the target surface, which causes deflection of the reflected vortex beam [64,65]. In the second type, the second-order harmonic photon does not obtain additional OAM, thus forming the CP Gaussian harmonic. This additional OAM is very likely to be transferred to the plasma to conserve the AM.

IV. DISCUSSION

The relative intensity of the VSH and GSH is closely related to the vortex and nonvortex driving sources in the E_x component [Eq. (2)], respectively. The vortex source, approximately $\cos\theta\,\partial_r u(r) e^{i(\omega_0 t + \sigma\varphi)}$, is remarkable in close-to-normal incidence ($\theta \simeq 0$), while the nonvortex source, approximately $\sin\theta e^{i\omega_0 t}$, on the contrary, prefers a large incident angle. In Fig. 4(a), we present the pure vortex photon number extracted from the second-order harmonic beam with incident angles from 0 to 10°. The laser energy is fixed here. The pure vortex photon accounts for about one half of the total second-order harmonic photons (denominator) in oblique incidence $\theta = 5°$, $n_e = 5n_c$, and becomes about 24% when $\theta = 10°$. Although this declines, the denominator increases rapidly, since the CP beams impose a fast oscillating component on the plasma surface in oblique incidence [52], so the absolute number of pure vortex photons is still very high. We see that the aforementioned pure vortex photon number, $N_{\mathrm{VSH}} = 1.66 \times 10^{13}$, at $\theta = 5°$ can reach 95.4% of that in normal incidence (1.74×10^{13}). This ratio is well preserved, reaching 77% for a larger angle of $\theta = 10°$.

A smaller laser focal spot, with a steeper slope of the envelope $\partial_r u(r)$, and thus, stronger vortex driving source, is still favored in oblique incidence, as in the normal case

[41]. As shown in Fig. 4(b), the proportion of vortex photons declines almost linearly at first and then becomes flat at large laser focal sizes. Increasing the laser focal size to 5 μm (electron density $5n_c$, incident angle 5°) reduces the proportion of vortex photons to 24% (50% for a laser spot of 2.5 μm).

At a higher plasma density of $100n_c$, where the target interface is less deformed [48], the proportion of pure vortex photons is similar to that at $5n_c$ [dashed lines in Fig. 4(a)], indicating that the generation efficiency of the vortex photons is insensitive to the plasma density at this moderate relativistic driving field of $a_0 = 2$. The total photon yield, however, declines in this case. At higher laser intensities, the relativistic self-induced transparency effect increases the density at which the laser field is reflected by $n_e = \langle\gamma\rangle n_c$, where the time-averaged $\langle\gamma\rangle = \sqrt{1+\langle a_0\rangle^2}$ is the relativistic factor for the laser beam [66]. The target will be more curved away from a flat surface, leading to a stronger vortex driving force [48] and more vortex harmonic photons. Simulation results show that the weight ratio of vortex and Gaussian second-order harmonics ascend to 1.82 (1.63) for E_y (E_z) at an incident laser amplitude of $a_0 = 10$ ($\theta = 5^\circ$, $n_e = 100n_c$). Simulations are also performed to show that the pulse duration has little effect on the proportion.

V. CONCLUSION

We investigate CP vortex harmonic generation when using a CP Gaussian laser beam obliquely impinging on a plasma target. The nth-order harmonic is composed of vortex modes with topological charges from $l = 0$ (Gaussian) to $|l| = n - 1$, the composition ratio of which is closely related to the laser focal size and the incident angle. For the case of a laser with a spot size of 2.5 μm, irradiating on the plasma target ($n_e = 5n_c$) at an incident angle of 5°, the mode contributions in the second-order harmonic are the vortex $l = 1$ and the Gaussian mode. The vortex component accounts for about one half of the total harmonic photon. Although the proportion declines with increasing incident angle, the absolute number of pure vortex photons is still comparable with that in normal incidence. Considering the difficulties faced by normal incidence, the fact that oblique incidence provides enough vortex photons with a relatively large angle tolerance make it viable for experiments and provides a feasible method to obtain intense vortex harmonics in real situations.

ACKNOWLEDGMENTS

This work is supported by the National Natural Science Foundation of China (Grants No. 61805266, No. 11935008, and No. 11922515), the Innovation Program of Shanghai Municipal Education Commission (Grant No. 201701070002E00032), the Ministry of Science and Technology of the People's Republic of China (Grants No. 2018YFA0404803 and No. 2016YFA0401102), the Strategic Priority Research Program of the Chinese Academy of Sciences (Grant No. XDB16), and the Natural Science Foundation of the Jiangsu Higher Education Institutions of China (Grant No. 18KJD140002). The authors acknowledge the open-source project postpic [67] for help with data analysis.

APPENDIX A: SIMULATION SETUP AND PHYSICAL QUANTITIES

In this section, we present the simulation setup in the x-o-y plane, as a supplement to Fig. 1(a), and the physical quantities, including the energy centroid, momentum, and total AM during the laser-plasma interaction process.

Figure 5(a) shows the E_z component of the incident CP Gaussian beam and the untouched-plane plasma target; the parameters are described in the main text. In Fig. 5(b), the field is completely reflected by the plasma target and leaves a dent in the latter. This reflection is accompanied by the HHG process. The green dots show the energy centroid of the electromagnetic (EM) field obtained from the energy density, $u = \frac{1}{2}[\epsilon_0\mathbf{E}^2 + (\mathbf{B}^2/\mu_0)]$; the blue arrows are the vector demonstration of the integrated momentum, $\mathbf{P} = \int_D \epsilon_0(\mathbf{E}\times\mathbf{B})dv$; and the red arrows represent the total AM. From the momentum, we see clearly the incident and reflection directions of the laser. As for the AM, its direction is the same as that of momentum on incidence but opposite after being reflected because the AM is pseudovector.

The main results in our paper (Figs. 1 to 3) are based on the EM field at the moment of Fig. 5(b), i.e., $t =$ 80.1 fs. The propagating direction of the laser at this time is 179.86°, obtained by P_y/P_x, and the energy centroid is

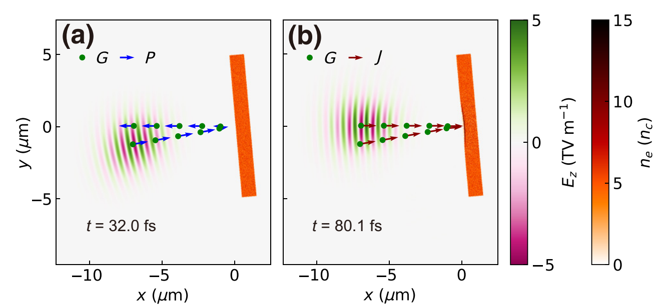

FIG. 5. Snapshot of E_z component and plasma target at (a) $t = 32.0$ fs (incident stage) and (b) $t = 80.1$ fs when the beam is completely reflected. Evolution of energy centroid (G, green dots), momentum (P, blue arrows), and total angular momentum (J, red arrows) of the electromagnetic field between $t = 32.0$ fs and 80.1 fs is also superposed.

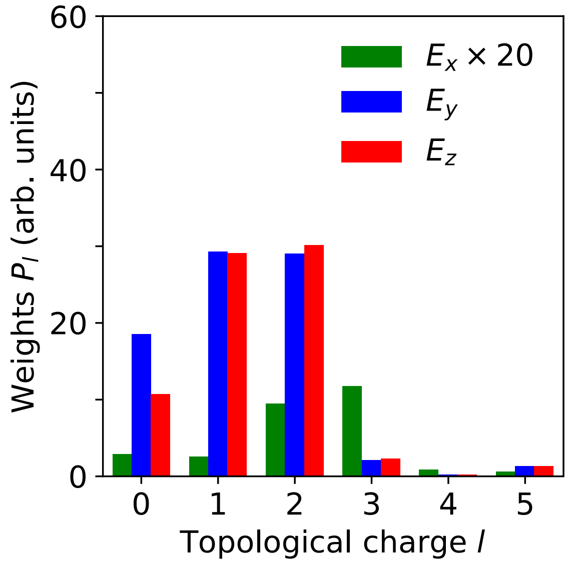

FIG. 6. OAM spectrum integrated along x direction of third-order harmonic.

$x = -6.95$ μm, $y = 0.05$ μm. These data indicate that the reflected light beam propagates along the $-x$ direction, as expected.

APPENDIX B: ANGULAR-MOMENTUM SPECTRUM OF THE THIRD-ORDER HARMONIC

This section presents the OAM spectrum of the third-order harmonic, as shown in Fig. 6. More OAM components, including CP Gaussian and CP vortex $l = 1$ and $l = 2$ modes are involved in building up the third-order harmonic. Figure 6, together with Fig. 2(b), verifies Eq. (7), such that, in the HHG scenario driven by an obliquely incident CP Gaussian beam, the maximum topological charge of the OAM in the nth-order harmonic is $|l| = n - 1$.

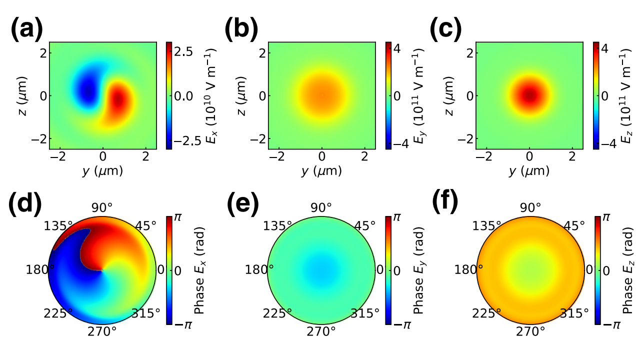

FIG. 7. Transverse slices of Gaussian mode in second-order harmonic: (a) E_x, (b) E_y, and (c) E_z; (d)–(f) corresponding phases. Slicing position is the same as that in the main text.

APPENDIX C: PROPERTIES OF THE GAUSSIAN PART IN THE SECOND-ORDER HARMONIC

This section presents the field and phase distributions of the Gaussian part in the second-order harmonic extracted by frequency selection from the field at $t = 80.1$ fs, as illustrated in Fig. 7. The transverse fields in Figs. 7(b) and 7(c) have typical Gaussian profiles and their phases are azimuthally uniform. The E_x component has a vortex wavefront, which results from circular polarization. The non-exact-zero phase in Figs. 7(e) and 7(f) is due to the propagating phase of the Gaussian beam.

[1] S. Pedersen, J. L. Herek, and A. H. Zewail, The validity of the “diradical” hypothesis: Direct femtoscond studies of the transition-state structures, Science **266**, 1359 (1994).

[2] C. Hernandez-Garcia, A. Picon, J. S. Roman, and L. Plaja, Attosecond Extreme Ultraviolet Vortices from High-Order Harmonic Generation, Phys. Rev. Lett. **111**, 083602 (2013).

[3] S. Patchkovskii and M. Spanner, High harmonics with a twist, Nat. Phys. **8**, 707 (2012).

[4] E. Goulielmakis, M. Schultze, M. Hofstetter, V. S. Yakovlev, J. Gagnon, M. Uiberacker, A. L. Aquila, E. M. Gullikson, D. T. Attwood, R. Kienberger, F. Krausz, and U. Kleineberg, Single-cycle nonlinear optics, Science **320**, 1614 (2008).

[5] X. Feng, S. Gilbertson, H. Mashiko, H. Wang, S. D. Khan, M. Chini, Y. Wu, K. Zhao, and Z. Chang, Generation of Isolated Attosecond Pulses with 20 to 28 Femtosecond Lasers, Phys. Rev. Lett. **103**, 183901 (2009).

[6] C. Winterfeldt, C. Spielmann, and G. Gerber, Colloquium: Optimal control of high-harmonic generation, Rev. Mod. Phys. **80**, 117 (2008).

[7] Y. Nomura, R. Hörlein, P. Tzallas, B. Dromey, S. Rykovanov, Z. Major, J. Osterhoff, S. Karsch, L. Veisz, M. Zepf, D. Charalambidis, F. Krausz, and G. D. Tsakiris, Attosecond phase locking of harmonics emitted from laser-produced plasmas, Nat. Phys. **5**, 124 (2008).

[8] S. V. Bulanov, N. M. Naumova, and F. Pegoraro, Interaction of an ultrashort, relativistically strong laser pulse with an overdense plasma, Phys. Plasmas **1**, 745 (1994).

[9] R. Lichters, J. Meyer-ter-Vehn, and A. Pukhov, Short-pulse laser harmonics from oscillating plasma surfaces driven at relativistic intensity, Phys. Plasmas **3**, 3425 (1996).

[10] T. Baeva, S. Gordienko, and A. Pukhov, Theory of high-order harmonic generation in relativistic laser interaction with overdense plasma, Phys. Rev. E **74**, 046404 (2006).

[11] B. Dromey, M. Zepf, A. Gopal, K. Lancaster, M. S. Wei, K. Krushelnick, M. Tatarakis, N. Vakakis, S. Moustaizis, R. Kodama, M. Tampo, C. Stoeckl, R. Clarke, H. Habara, D. Neely, S. Karsch, and P. Norreys, High harmonic generation in the relativistic limit, Nat. Phys. **2**, 456 (2006).

[12] A. Pukhov, X-rays in a flash, Nat. Phys. **2**, 439 (2006).

[13] B. Dromey, S. Kar, C. Bellei, D. C. Carroll, R. J. Clarke, J. S. Green, S. Kneip, K. Markey, S. R. Nagel, P. T. Simpson, L. Willingale, P. McKenna, D. Neely, Z. Najmudin, K. Krushelnick, P. A. Norreys, and M. Zepf, Bright

Multi-keV Harmonic Generation From Relativistically Oscillating Plasma Surfaces, Phys. Rev. Lett. **99**, 085001 (2007).

[14] Y. Pertot, C. Schmidt, M. Matthews, A. Chauvet, M. Huppert, V. Svoboda, A. von Conta, A. Tehlar, D. Baykusheva, J.-P. Wolf, and H. J. Wörner, Time-resolved X-ray absorption spectroscopy with a water window high-harmonic source, Science **355**, 264 (2017).

[15] S. X. Hu and L. A. Collins, Attosecond Pump Probe: Exploring Ultrafast Electron Motion Inside an Atom, Phys. Rev. Lett. **96**, 073004 (2006).

[16] O. Renner and F. B. Rosmej, Challenges of X-ray spectroscopy in investigations of matter under extreme conditions, Matter Radiat. Extrem. **4**, 024201 (2019).

[17] M. Lara-Astiaso, M. Galli, A. Trabattoni, A. Palacios, D. Ayuso, F. Frassetto, L. Poletto, S. D. Camillis, J. Greenwood, P. Decleva, I. Tavernelli, F. Calegari, M. Nisoli, and F. Martín, Attosecond pump–probe spectroscopy of charge dynamics in tryptophan, J. Phys. Chem. Lett. **9**, 4570 (2018).

[18] F. Calegari, D. Ayuso, A. Trabattoni, L. Belshaw, S. D. Camillis, S. Anumula, F. Frassetto, L. Poletto, A. Palacios, P. Decleva, J. B. Greenwood, F. Martin, and M. Nisoli, Ultrafast electron dynamics in phenylalanine initiated by attosecond pulses, Science **346**, 336 (2014).

[19] E. J. Takahashi, P. Lan, O. D. Mucke, Y. Nabekawa, and K. Midorikawa, Nonlinear attosecond metrology by intense isolated attosecond pulses, IEEE J. Sel. Top Quantum Electron. **21**, 1 (2015).

[20] J. H. Poynting, The wave motion of a revolving shaft, and a suggestion as to the angular momentum in a beam of circularly polarised light, Proc. R. Soc. London, A: Contain. Pap. Math. Phys. Charact. **82**, 560 (1909).

[21] R. A. Beth, Mechanical detection and measurement of the angular momentum of light, Phys. Rev. **50**, 115 (1936).

[22] L. Allen, M. W. Beijersbergen, R. J. C. Spreeuw, and J. P. Woerdman, Orbital angular momentum of light and the transformation of Laguerre-Gaussian laser modes, Phys. Rev. A **45**, 8185 (1992).

[23] L. Marrucci, C. Manzo, and D. Paparo, Optical Spin-To-Orbital Angular Momentum Conversion in Inhomogeneous Anisotropic Media, Phys. Rev. Lett. **96**, 163905 (2006).

[24] N. R. Heckenberg, R. McDuff, C. P. Smith, and A. G. White, Generation of optical phase singularities by computer-generated holograms, Opt. Lett. **17**, 221 (1992).

[25] Y. Shi, B. Shen, L. Zhang, X. Zhang, W. Wang, and Z. Xu, Light Fan Driven by a Relativistic Laser Pulse, Phys. Rev. Lett. **112**, 235001 (2014).

[26] J. Vieira, R. M. Trines, E. P. Alves, R. A. Fonseca, J. T. Mendonca, R. Bingham, P. Norreys, and L. O. Silva, Amplification and generation of ultra-intense twisted laser pulses via stimulated Raman scattering, Nat. Commun. **7**, 10371 (2016).

[27] A. Leblanc, A. Denoeud, L. Chopineau, G. Mennerat, P. Martin, and F. Quéré, Plasma holograms for ultrahigh-intensity optics, Nat. Phys. **13**, 440 (2017).

[28] Y.-Y. Chen, K. Z. Hatsagortsyan, and C. H. Keitel, Generation of twisted γ-ray radiation by nonlinear Thomson scattering of twisted light, Matter Radiat. Extrem. **4**, 024401 (2019).

[29] W. Pan, X. Liang, L. Yu, A. Wang, J. Li, and R. Li, Generation of terawatt-scale vortex pulses based on optical parametric chirped-pulse amplification, IEEE Photonics J. **12**, 1 (2020).

[30] J. Qian, Y. Peng, Y. Li, P. Wang, B. Shao, Z. Liu, Y. Leng, and R. Li, Femtosecond mid-ir optical vortex laser based on optical parametric chirped pulse amplification, Photonics Res. **8**, 421 (2020).

[31] H. He, M. E. J. Friese, N. R. Heckenberg, and H. Rubinsztein-Dunlop, Direct Observation of Transfer of Angular Momentum to Absorptive Particles from a Laser Beam with a Phase Singularity, Phys. Rev. Lett. **75**, 826 (1995).

[32] M. Padgett and R. Bowman, Tweezers with a twist, Nat. Photonics **5**, 343 (2011).

[33] S. Fürhapter, A. Jesacher, S. Bernet, and M. Ritsch-Marte, Spiral interferometry, Opt. Lett. **30**, 1953 (2005).

[34] J. Leach, B. Jack, J. Romero, A. K. Jha, A. M. Yao, S. Franke-Arnold, D. G. Ireland, R. W. Boyd, S. M. Barnett, and M. J. Padgett, Quantum correlations in optical angle-orbital angular momentum variables, Science **329**, 662 (2010).

[35] J. Wang, J.-Y. Yang, I. M. Fazal, N. Ahmed, Y. Yan, H. Huang, Y. Ren, Y. Yue, S. Dolinar, M. Tur, and A. E. Willner, Terabit free-space data transmission employing orbital angular momentum multiplexing, Nat. Photonics **6**, 488 (2012).

[36] X. Zhang, B. Shen, Y. Shi, X. Wang, L. Zhang, W. Wang, J. Xu, L. Yi, and Z. Xu, Generation of Intense High-Order Vortex Harmonics, Phys. Rev. Lett. **114**, 173901 (2015).

[37] A. Denoeud, L. Chopineau, A. Leblanc, and F. Quere, Interaction of Ultraintense Laser Vortices with Plasma Mirrors, Phys. Rev. Lett. **118**, 033902 (2017).

[38] F. Kong, C. Zhang, F. Bouchard, Z. Li, G. G. Brown, D. H. Ko, T. J. Hammond, L. Arissian, R. W. Boyd, E. Karimi, and P. B. Corkum, Controlling the orbital angular momentum of high harmonic vortices, Nat. Commun. **8**, 14970 (2017).

[39] D. Gauthier, P. R. Ribič, G. Adhikary, A. Camper, C. Chappuis, R. Cucini, L. F. DiMauro, G. Dovillaire, F. Frassetto, R. Géneaux, P. Miotti, L. Poletto, B. Ressel, C. Spezzani, M. Stupar, T. Ruchon, and G. De Ninno, Tunable orbital angular momentum in high-harmonic generation, Nat. Commun. **8**, 14971 (2017).

[40] L. Ji, B. Shen, X. Zhang, M. Wen, C. Xia, W. Wang, J. Xu, Y. Yu, M. Yu, and Z. Xu, Ultra-intense single attosecond pulse generated from circularly polarized laser interacting with overdense plasma, Phys. Plasmas **18**, 083104 (2011).

[41] S. Li, X. Zhang, W. Gong, Z. Bu, and B. Shen, Spin-to-orbital angular momentum conversion in harmonic generation driven by intense circularly polarized laser, New J. Phys. **22**, 013054 (2020).

[42] Y. Zhao, J. S. Edgar, G. D. M. Jeffries, D. McGloin, and D. T. Chiu, Spin-To-Orbital Angular Momentum Conversion in a Strongly Focused Optical Beam, Phys. Rev. Lett. **99**, 073901 (2007).

[43] G. F. Quinteiro, F. Schmidt-Kaler, and C. T. Schmiegelow, Twisted-Light–Ion Interaction: The Role of Longitudinal Fields, Phys. Rev. Lett. **119**, 253203 (2017).

[44] K. Y. Bliokh, F. J. Rodríguez-Fortuño, F. Nori, and A. V. Zayats, Spin–orbit interactions of light, Nat. Photonics **9**, 796 (2015).

[45] J. Ren, Y. Li, Y. Lin, Y. Qin, R. Wu, J. Yang, Y.-F. Xiao, H. Yang, and Q. Gong, Spin hall effect of light reflected from a magnetic thin film, Appl. Phys. Lett. **101**, 171103 (2012).

[46] K. Y. Bliokh, M. A. Alonso, E. A. Ostrovskaya, and A. Aiello, Angular momenta and spin-orbit interaction of non-paraxial light in free space, Phys. Rev. A **82**, 063825 (2010).

[47] K. Y. Bliokh, A. Y. Bekshaev, and F. Nori, Extraordinary momentum and spin in evanescent waves, Nat. Commun. **5**, 3300 (2014).

[48] J. W. Wang, M. Zepf, and S. G. Rykovanov, Intense attosecond pulses carrying orbital angular momentum using laser plasma interactions, Nat. Commun. **10**, 5554 (2019).

[49] B. Feng, C. Y. Qin, X. S. Geng, Q. Yu, W. Q. Wang, Y. T. Wu, X. Yan, L. L. Ji, and B. F. Shen, The emission of γ-Ray beams with orbital angular momentum in laser-driven micro-channel plasma target, Sci. Rep. **9**, 18780 (2019).

[50] L. Yi, High-Harmonic Generation and Spin-Orbit Interaction of Light in a Relativistic Oscillating Window, Phys. Rev. Lett. **126**, 134801 (2021).

[51] A. A. M. Cuyt, V. Petersen, B. Verdonk, H. Waadeland, and W. B. Jones, *Handbook of Continued Fractions for Special Functions* (Springer Netherlands, Dordrecht, 2008).

[52] Z. Y. Chen and A. Pukhov, Bright high-order harmonic generation with controllable polarization from a relativistic plasma mirror, Nat. Commun. **7**, 12515 (2016).

[53] T. D. Arber, K. Bennett, C. S. Brady, A. Lawrence-Douglas, M. G. Ramsay, N. J. Sircombe, P. Gillies, R. G. Evans, H. Schmitz, A. R. Bell, and C. P. Ridgers, Contemporary particle-in-cell approach to laser-plasma modelling, Plasma Phys. Controlled Fusion **57**, 113001 (2015).

[54] V. A. Pas'ko, I. V. Basistiy, M. V. Vasnetsov, and M. S. Soskin, in *Sixth International Conference on Correlation Optics*, Vol. 5477 (SPIE, Chernivsti, 2004), p. 83.

[55] A. D'Errico, R. D'Amelio, B. Piccirillo, F. Cardano, and L. Marrucci, Measuring the complex orbital angular momentum spectrum and spatial mode decomposition of structured light beams, Optica **4**, 1350 (2017).

[56] G. Pariente and F. Quéré, Spatio-temporal light springs: Extended encoding of orbital angular momentum in ultrashort pulses, Opt. Lett. **40**, 2037 (2015).

[57] C. Wagner and N. Harned, Lithography gets extreme, Nat. Photonics **4**, 24 (2010).

[58] G. Tallents, E. Wagenaars, and G. Pert, Lithography at EUV wavelengths, Nat. Photonics **4**, 809 (2010).

[59] S. Tao, X.-C. Yuan, J. Lin, X. Peng, and H. Niu, Fractional optical vortex beam induced rotation of particles, Opt. Express **13**, 7726 (2005).

[60] C. Fallet, J. Caron, S. Oddos, J.-Y. Tinevez, L. Moisan, G. Y. Sirat, P. O. Braitbart, and S. L. Shorte, in *Nanoimaging and Nanospectroscopy II*, Vol. 9169, edited by P. Verma and A. Egner (SPIE, San Diego, California, 2014), p. 916905.

[61] A. Blinne, S. Kuschel, S. Tietze, and M. Zepf, Efficient retrieval of phase information from real-valued electromagnetic field data, J. Comput. Phys.: X **1**, 100019 (2019).

[62] J. Leach, M. J. Padgett, S. M. Barnett, S. Franke-Arnold, and J. Courtial, Measuring the Orbital Angular Momentum of a Single Photon, Phys. Rev. Lett. **88**, 257901 (2002).

[63] L. Rego, J. S. Roman, A. Picon, L. Plaja, and C. Hernandez-Garcia, Nonperturbative Twist in the Generation of Extreme-Ultraviolet Vortex Beams, Phys. Rev. Lett. **117**, 163202 (2016).

[64] L. Zhang, B. Shen, X. Zhang, S. Huang, Y. Shi, C. Liu, W. Wang, J. Xu, Z. Pei, and Z. Xu, Deflection of a Reflected Intense Vortex Laser Beam, Phys. Rev. Lett. **117**, 113904 (2016).

[65] Y. H. Tang, Z. Gong, J. Q. Yu, Y. R. Shou, and X. Q. Yan, Deflection of a reflected intense circularly polarized light beam induced by asymmetric radiation pressure, Phys. Rev. E **100**, 063203 (2019).

[66] L. Willingale, S. R. Nagel, A. G. R. Thomas, C. Bellei, R. J. Clarke, A. E. Dangor, R. Heathcote, M. C. Kaluza, C. Kamperidis, S. Kneip, K. Krushelnick, N. Lopes, S. P. D. Mangles, W. Nazarov, P. M. Nilson, and Z. Najmudin, Characterization of High-Intensity Laser Propagation in the Relativistic Transparent Regime Through Measurements of Energetic Proton Beams, Phys. Rev. Lett. **102**, 125002 (2009).

[67] https://github.com/skuschel/postpic.